

## Article

# Enhanced Gas Sensing Performance of ZnO/Ti<sub>3</sub>C<sub>2</sub>T<sub>x</sub> MXene Nanocomposite

Qui Thanh Hoai Ta <sup>1,†</sup>, Deepika Thakur <sup>2,†</sup> and Jin-Seo Noh <sup>1,\*</sup><sup>1</sup> Department of Physics, Gachon University, 1342 Seongnamdaero, Sujeong-gu, Seongnam-si 13120, Korea<sup>2</sup> Department of Agriculture, Forestry and Bioresources, Seoul National University, 1 Gwanak-ro, Gwanak-gu, Seoul 08826, Korea

\* Correspondence: jinseonoh@gachon.ac.kr; Tel.: +82-317505611

† These authors contributed equally to this work.

**Abstract:** A representative of titanium carbide MXene, Ti<sub>3</sub>C<sub>2</sub>T<sub>x</sub> is a promising candidate for high performance gas sensing and has attracted significant attention. However, MXene naturally has a multilayer structure with low porosity, which prevents its gas-sensing activity. Zinc oxide (ZnO) has long been utilized as a gas detector. Despite its good response to multiple gases, high operation temperature has limited its widespread use as a gas-sensing material. In this study, a room-temperature toxic gas sensor was prepared from ZnO/Ti<sub>3</sub>C<sub>2</sub>T<sub>x</sub> MXene nanocomposite consisting of 2D few-layered MXene and 1D ZnO nanoparticles. A simple technique for synthesizing the nanocomposite was established. The physicochemical properties of the nanocomposite were fine-controlled with more active sites and higher porosity. The sensitivity and gas-selectivity of the sensing material were closely examined. The nanocomposite showed enhanced response and recovery behaviors to toxic gases, which outperformed pure Ti<sub>3</sub>C<sub>2</sub>T<sub>x</sub> MXene and pure ZnO. This study offers a practical strategy by which to increase the gas-sensing performance of Ti<sub>3</sub>C<sub>2</sub>T<sub>x</sub> MXene, and expands comprehensive understanding of the gas-sensing process of ZnO/Ti<sub>3</sub>C<sub>2</sub>T<sub>x</sub> p-n heterostructure.



**Citation:** Ta, Q.T.H.; Thakur, D.; Noh, J.-S. Enhanced Gas Sensing Performance of ZnO/Ti<sub>3</sub>C<sub>2</sub>T<sub>x</sub> MXene Nanocomposite. *Micromachines* **2022**, *13*, 1710. <https://doi.org/10.3390/mi13101710>

Academic Editor: Nityasagar JENA

Received: 13 September 2022

Accepted: 10 October 2022

Published: 11 October 2022

**Publisher's Note:** MDPI stays neutral with regard to jurisdictional claims in published maps and institutional affiliations.



**Copyright:** © 2022 by the authors. Licensee MDPI, Basel, Switzerland. This article is an open access article distributed under the terms and conditions of the Creative Commons Attribution (CC BY) license (<https://creativecommons.org/licenses/by/4.0/>).

**Keywords:** Ti<sub>3</sub>C<sub>2</sub>T<sub>x</sub> MXene; ZnO; nanocomposite; gas sensor

## 1. Introduction

MXenes, also known as two-dimensional (2D) carbides, nitrides, and carbonitrides, have gained huge attention due to their unique surface properties, morphology, and potential applications [1–3]. MXenes are represented by the general formula: M<sub>n+1</sub>X<sub>n</sub>T<sub>x</sub> (n = 1–4), where M stands for transition metals, X stands for carbon or nitrogen, and T<sub>x</sub> holds for a functional group such as fluorine, hydroxyl, and oxygen [4–6]. Mostly, MXenes have been researched for gas sensing due to the ease of tuning the surface termination groups. Among various MXenes, titanium carbide (Ti<sub>3</sub>C<sub>2</sub>T<sub>x</sub> MXene) has been studied the most, due to its high electron density and sensitive interactions with toxic gas molecules [2,7,8].

However, while MXenes have been proven to be useful, their poor stability in humid environments and loss in surface area after hydration limit its potential applications [9–11]. In addition, low-porosity and high operating temperatures have caused various complications during their synthesis process [12,13]. This is why there is a need for the incorporation of other materials in combination with pure MXenes.

Some efforts have been made by scientists to sensitize Ti<sub>3</sub>C<sub>2</sub>T<sub>x</sub> MXene [14–17]. In our previous study, we synthesized Si-doped TiO<sub>2</sub>/Ti<sub>3</sub>C<sub>2</sub>T<sub>x</sub> hybridstructure using a diffusion process of Si atom at 1000 °C for enhancing NO<sub>2</sub> sensing activity [18]. Zhao et al. explored PANI/Ti<sub>3</sub>C<sub>2</sub>T<sub>x</sub> nanocomposite to enhance ethanol sensing properties [19]. In 2021, Yang et al. studied crumpled ZnO/Ti<sub>3</sub>C<sub>2</sub>T<sub>x</sub> sphere, using ultrasonic spray pyrolysis technique to improve the NO<sub>2</sub> sensing performance [20]. In fact, in these previous works, a certain unilateral parameter of the sensor was enhanced. The comprehensive sensing activity of the response and recovery values should therefore be further improved [21,22].

In this work, we have highlighted the enhanced gas sensing performance of ZnO/Ti<sub>3</sub>C<sub>2</sub>T<sub>x</sub> MXene nanocomposite at room-temperature. To increase the surface area of the material, we incorporated 1D ZnO nanoparticles on the surface of 2D few-layered MXene. The ZnO/Ti<sub>3</sub>C<sub>2</sub>T<sub>x</sub> MXene nanocomposite significantly improved the performance for toxic gas sensing. In addition, it was found that the response and recovery time of the ZnO/Ti<sub>3</sub>C<sub>2</sub>T<sub>x</sub> MXene nanocomposite outperformed the pure ZnO NPs and Ti<sub>3</sub>C<sub>2</sub>T<sub>x</sub> MXene. Furthermore, the gas-sensing process of ZnO/Ti<sub>3</sub>C<sub>2</sub>T<sub>x</sub> p-n heterostructure revealed better stability and performance than Ti<sub>3</sub>C<sub>2</sub>T<sub>x</sub> MXene in gas sensing.

## 2. Materials and Methods

### 2.1. Materials and Chemicals

Ti<sub>3</sub>AlC<sub>2</sub> powder was provided by 11 Technology Company (China). Zinc acetate dihydrate (Zn(CH<sub>3</sub>COO)<sub>2</sub>•2H<sub>2</sub>O), potassium hydroxide (KOH), and methanol (CH<sub>3</sub>OH) were obtained from Sigma-Aldrich (St. Louis, MO, USA). Hydrofluoric acid (HF, 48–51%) was bought from Fisher Scientific (Ward Hill, MA, USA). Ethyl alcohol (C<sub>2</sub>H<sub>5</sub>OH) was purchased from Daejung Chem (Gyeonggi-do, Korea). All the chemicals were used as provided without any further treatment.

### 2.2. Preparation of Ti<sub>3</sub>C<sub>2</sub>T<sub>x</sub> MXene and ZnO/Ti<sub>3</sub>C<sub>2</sub>T<sub>x</sub> Nanocomposites

First, multilayered Ti<sub>3</sub>C<sub>2</sub>T<sub>x</sub> MXenes were prepared by selectively etching Al layers from the pristine Ti<sub>3</sub>AlC<sub>2</sub> powder. Typically, a 2.0 g of pristine Ti<sub>3</sub>AlC<sub>2</sub> MAX phase was gradually immersed into 56 mL of a concentrated HF under continuous stirring at 300 rpm in an ice bath to avoid heat generation, and the mixed solution was transferred to an oil bath at 50 °C [23,24]. After one day of reaction, the MXene multilayer structures were collected and washed several times with DI water. Subsequently, a sample of few-layered Ti<sub>3</sub>C<sub>2</sub>T<sub>x</sub> MXene was prepared by ultrasonic probe sonicator (Sonics & Materials INC, Newtown, CT, USA) for around 30 min using multilayered MXene. Then, the obtained precipitate was dried overnight using a freeze-drying system (ilShinBioBase Co. Ltd., Gyeonggi-do, Korea) for further experiments.

ZnO/Ti<sub>3</sub>C<sub>2</sub>T<sub>x</sub> nanocomposites were synthesized by a simple technique, as schematically shown in Figure 1. Briefly, varying amounts (100, 200, and 300 mg) of the few-layered Ti<sub>3</sub>C<sub>2</sub>T<sub>x</sub> MXene powders were added to 25 mL of Zn<sup>2+</sup> solution. A total of 340 mg of KOH was dispersed in 15 mL of methanol under heat [25]. Subsequently, the two solutions were mixed to give the final precursor solution, which was kept under heat and sonication to form ZnO nanoparticles. After 30 min of reaction, the obtained products were continuously washed to remove the byproducts and named following real ratio as ZT1 (163:100), ZT2 (163:200), and ZT3 (163:300), respectively. Moreover, the pure ZnO nanoparticles were prepared for comparison in the same parameters without any Ti<sub>3</sub>C<sub>2</sub>T<sub>x</sub> MXene.

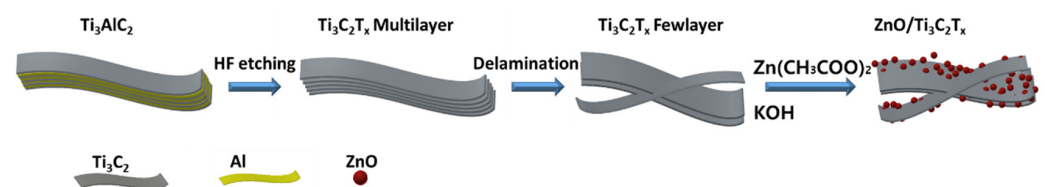


**Figure 1.** Schematic synthesis procedure of ZnO/Ti<sub>3</sub>C<sub>2</sub>T<sub>x</sub> heterostructure.

### 2.3. Characterizations and Gas Sensing Measurements

The X-ray diffraction (XRD) patterns of as-prepared samples were obtained using a high resolution X-ray diffractometer (Rigaku, SmartLab, Tokyo, Japan) equipped with 3 kW Cu K $\alpha$  radiation. The morphology of all samples was collected using scanning electron microscopy (FESEM, Hitachi, S-4700, Tokyo, Japan) and high resolution transmission electron microscopy (HR-TEM, Tecnai, Hillsboro, OR, USA). The bonding states and surface characteristics of selected samples were analyzed by X-ray photoelectron spectroscopy (XPS, K $\alpha$  plus, Thermo Fisher Scientific, Waltham, MA, USA). The Brunauer-Emmett-Teller (BET)

analysis was measured using a nitrogen adsorption-desorption system (Micromeritics, ASAP 2020, Norcross, GA, USA).

To achieve gas sensing properties, concentrated suspensions of the as-prepared samples were covered on a glass substrate ( $10 \times 10$  mm). The gas sensing measurements were measured in a stainless-steel chamber ( $682 \text{ cm}^3$ ) at room temperature. The real-time resistance of the samples, when exposed to the toxic target gas ( $R_g$ ) and synthetic air ( $R_a$ ), was measured through Au wires using a digital source measure unit (SMU, Keithley 2450) [26]. Five target gases ( $\text{CO}_2$ ,  $\text{H}_2$ ,  $\text{CH}_4$ ,  $\text{NH}_3$ , and  $\text{NO}_2$ ) were used as the tested gases at high and low humidity ambient. The different gas concentrations of the toxic gas were produced by mixing it with synthetic air using a flow and pressure controller (GMC 1200). The gas sensor response value of the nanocomposite was expressed using the following equation [27]:

$$\text{Response (\%)} = (R_g - R_a) \times 100/R_a, \quad (1)$$

### 3. Results and Discussion

#### 3.1. Microstructures and Structural Components

Observation of morphological surfaces of the  $\text{Ti}_3\text{AlC}_2$  MAX phase,  $\text{Ti}_3\text{C}_2\text{T}_x$  MXene, pure ZnO nanoparticles, and ZnO/ $\text{Ti}_3\text{C}_2\text{T}_x$  nanocomposite were analyzed using FESEM with high- and low-magnification (FESEM, Hitachi, S-4700, Tokyo, Japan). As displayed in Figure 2a, the pristine MAX phase has terraced microstructures with an average grain below  $8 \mu\text{m}$ . After etching the MAX phase in concentrated HF solution, the micromorphology of multilayered  $\text{Ti}_3\text{C}_2\text{T}_x$  MXene accounts for an accordion-like sandwich, which exhibited successful Al-selective etching (Figure 2b). After sonicating the MXene multilayer for 30 min, a few-layered  $\text{Ti}_3\text{C}_2\text{T}_x$  MXene were regularly obtained. It can be observed from the inset magnified image in Figure 2c that the thickness of the  $\text{Ti}_3\text{C}_2\text{T}_x$  MXene was around 150–350 nm, which could be due to the few-layered  $\text{Ti}_3\text{C}_2\text{T}_x$  MXene. The as-synthesized ZnO displayed a particle shape with a diameter of 60–100 nm, as shown in Figure 2d. Compared to the pure ZnO nanoparticles, the few-layered  $\text{Ti}_3\text{C}_2\text{T}_x$  MXene might suppress the growth and accumulation of ZnO nanoparticles. The heterostructure could support, not only faster, but also excess diffusion paths for toxic target gases.

By focusing in further, the SEM image of ZnO/ $\text{Ti}_3\text{C}_2\text{T}_x$  nanocomposite clearly showed that the ZnO exhibited particle morphology, and featured a side anchored freely on the MXene two sides, suggesting efficient assembly between few-layered  $\text{Ti}_3\text{C}_2\text{T}_x$  MXene sheets and ZnO particles during the treatment process (Figure 2e,f). It was estimated that a single-layer  $\text{Ti}_3\text{C}_2\text{T}_x$  flake (2 nm thick) and few-layer (2–5 nm thick) flakes. The SEM and elemental mapping measurements of ZnO/ $\text{Ti}_3\text{C}_2\text{T}_x$  heterostructure (ZT2) suggested the presence of C, O, Ti, and Zn components in the nanocomposite. They displayed a highly homogeneous distribution of C, O, Ti, and Zn (Figure 3a). Moreover, the EDX spectrum also exhibited obvious C, O, Ti, and Zn elements, which were valuable for the stability and performance of the nanocomposite. As presented in Figure 3b,c, the HR-TEM images demonstrated the modification between the two interfaces, where both  $\text{Ti}_3\text{C}_2\text{T}_x$  MXenes and ZnO were cross-linked to each other. This local communication could enhance the interaction between electrons and gas molecules.

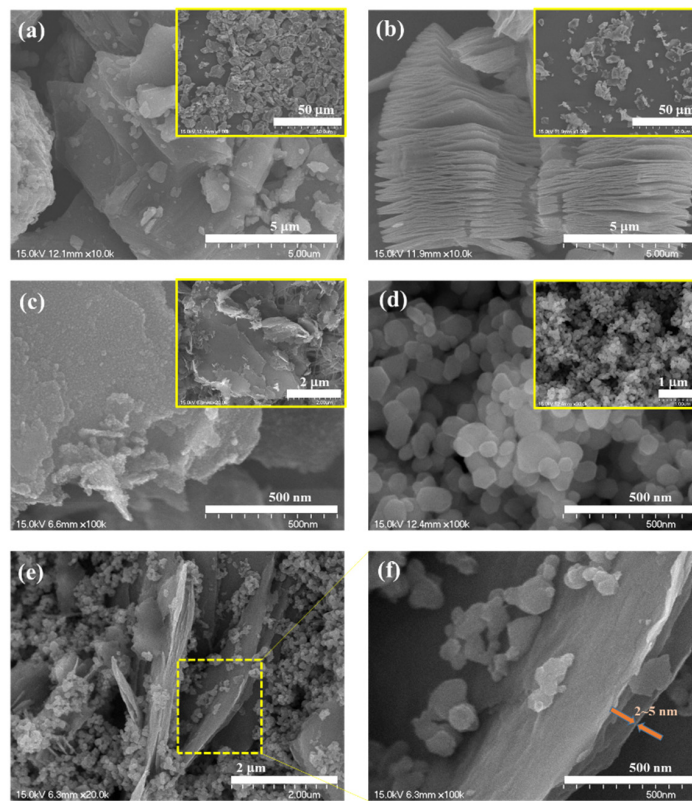


**Figure 2.** SEM images of (a)  $Ti_3AlC_2$  MAX phase, (b)  $Ti_3C_2T_x$  MXene multilayer, (c)  $Ti_3C_2T_x$  MXene few-layer, (d) pure ZnO nanoparticles, and (e,f) ZnO/ $Ti_3C_2T_x$  hybrid structure. The insets show low-magnification SEM images.

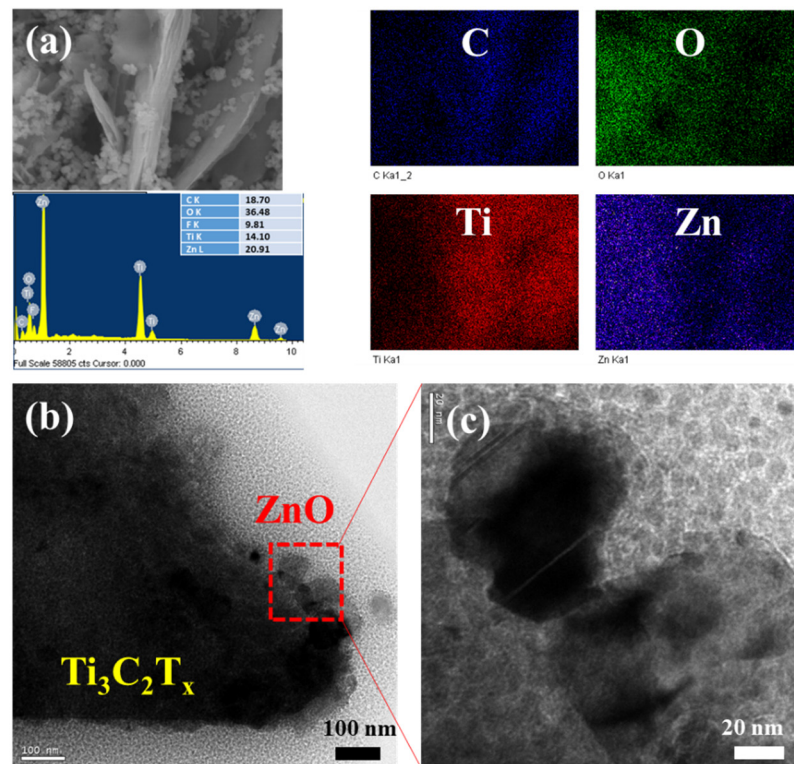


**Figure 3.** (a) SEM images and EDX spectrum with EDX element maps of Ti, C, O, Zn, and (b,c) HR-TEM images of ZnO/ $Ti_3C_2T_x$  heterostructure.

The XRD patterns of prepared samples are displayed in Figure 4a. Well-defined diffraction peaks can be seen at  $2\theta = 9.5^\circ$ ,  $19.1^\circ$ ,  $36.7^\circ$ ,  $38.7^\circ$ ,  $38.9^\circ$ , and  $60.1^\circ$ , which are indexed to the planes (002), (004), (101), (104), (105), (110), respectively (JCPDS card No.52-0875) [16]. After the etching development, a remarkable peak (002) in pure  $\text{Ti}_3\text{C}_2\text{T}_x$  MXene exhibits that Al was successfully corroded from the  $\text{Ti}_3\text{AlC}_2$  MAX phase. The chemical bonding between each layer was decreased by increasing the  $c$  parameter. Meanwhile, ZnO showed preferred growth in the (101) orientation in the nanocomposite, and prominent ZnO peaks were also observed at  $2\theta = 31.7^\circ$  and  $34.4^\circ$ , which were indexed to (100) and (002) planes, respectively. These peaks corresponded with the pure ZnO and the wurtzite structure (JCPDS card No.36-1451) [28]. The absence of any  $\text{TiO}_2$  peaks revealed that oxidation seemed to not occur in the combination procedure. Thus, the XRD results of synthesized samples were completely expected. As displayed in Figure 4b, both samples illustrated a type IV isotherm plot with a relative pressure from 0.42 to 1.0, indicating H3-type hysteresis circles [29]. Moreover, the BET-specific surface area (SSA) of  $\text{ZnO}/\text{Ti}_3\text{C}_2\text{T}_x$  was calculated to be  $29.7 \text{ m}^2/\text{g}$ , which is a 3.9-fold increase compared with the SSA of the  $\text{Ti}_3\text{C}_2\text{T}_x$  MXene ( $7.5 \text{ m}^2/\text{g}$ ). The results evidenced that the SSA of  $\text{ZnO}/\text{Ti}_3\text{C}_2\text{T}_x$  nanocomposite was significantly improved owing to ultra-sonication and decoration, which were expected to improve the active sites and enhance the transportation of electrons.

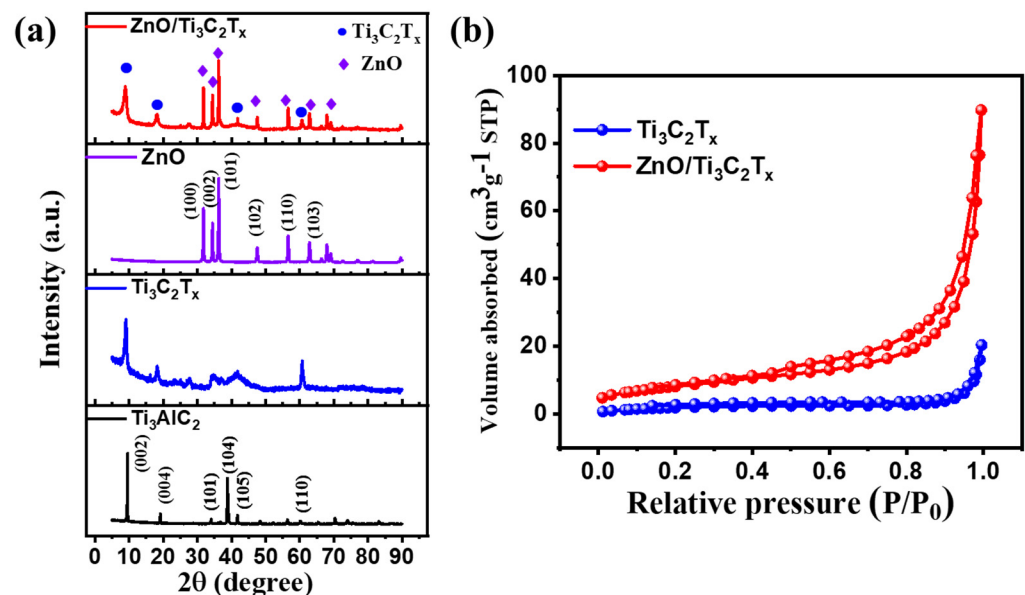


**Figure 4.** (a) XRD patterns of the  $\text{Ti}_3\text{AlC}_2$  MAX phase,  $\text{Ti}_3\text{C}_2\text{T}_x$  MXene, pure ZnO, and  $\text{ZnO}/\text{Ti}_3\text{C}_2\text{T}_x$  nanocomposite. (b)  $\text{N}_2$  adsorption-desorption isotherms for  $\text{Ti}_3\text{C}_2\text{T}_x$  MXene, and  $\text{ZnO}/\text{Ti}_3\text{C}_2\text{T}_x$  nanocomposite.

### 3.2. Chemical Binding States

The surface chemical and binding energy of  $\text{ZnO}/\text{Ti}_3\text{C}_2\text{T}_x$  nanocomposite was observed in detail using XPS measurement for Ti 2p, C 1s, Zn 2p, and O 1s. The results are displayed in Figure 5. The overall XPS survey spectrum of  $\text{ZnO}/\text{Ti}_3\text{C}_2\text{T}_x$  heterostructure is illustrated in Figure 5a, indicating the existence of Zn 2p, O 1s, Ti 2p, and C 1s. Meanwhile, Figure 5b–e reveals the various focused XPS spectra of individual elements. Figure 5b, showing a Ti 2p XPS spectra, indicates peaks at 454.9, 458.8, and 461.08 eV, corresponding to Ti-C, Ti-C and Ti-O, which may originate from  $\text{C-Ti}^{3+}\text{-T}_x$  and  $\text{C-Ti}^{2+}\text{-T}_x$  with  $\text{T}_x = \text{-OH}$ ,  $\text{-O-}$ ,  $\text{-F}$ , respectively [30]. Figure 5c reveals the C 1s high-resolution spectrum, fitted using two main components at 284.7 and 281.2 eV, which could originate from graphitic  $\text{C=C}$ , and C-Ti with a surface termination group, respectively [31]. Additionally, two main electronic states of Zn 2p, shown in Figure 5d, spotted at 1045.9 and 1023.0 eV by a spin separation of 22.9 eV, are assigned to Zn 2p<sub>1/2</sub> and Zn 2p<sub>3/2</sub>, respectively [20]. As

shown in Figure 5e, the O 1s high-resolution spectrum of the nanocomposite exhibited that the two prominent binding energy peaks at 530.2 and 532.2 eV could be assigned to O-Ti and C-Ti-T<sub>x</sub> (T<sub>x</sub> = -OH), respectively [32]. Therefore, the above results could deduce that the optimized nanocomposite exhibited an enhanced gas sensing performance.

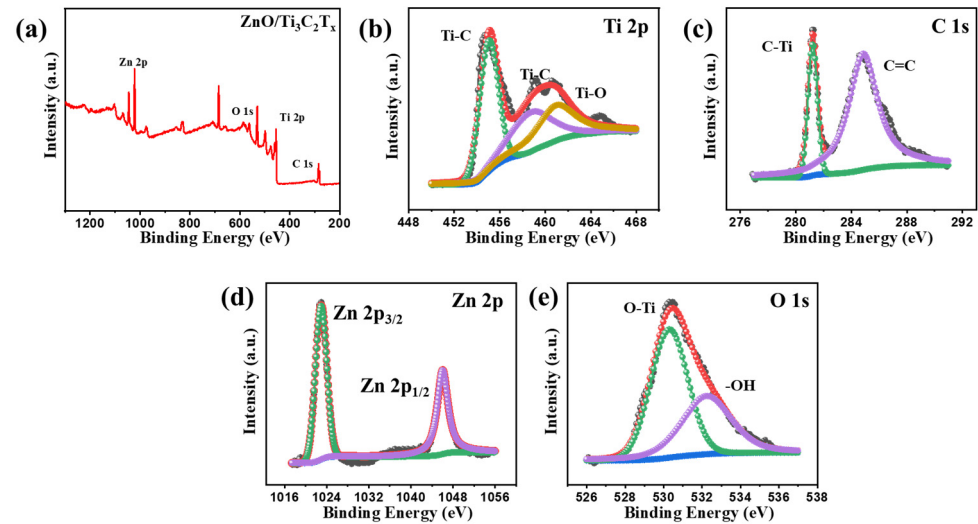


**Figure 5.** (a) Overall XPS spectrum of ZnO/Ti<sub>3</sub>C<sub>2</sub>T<sub>x</sub> nanocomposite (ZT2). Focused XPS spectra of (b) Ti 2p, (c) C 1s, (d) Zn 2p, and (e) O 1s, respectively.

### 3.3. Gas Sensing Performance and Sensing

In order to find the performance of the excellent gas-sensitive and selective activity of ZnO/Ti<sub>3</sub>C<sub>2</sub>T<sub>x</sub> nanocomposite, the gas sensing activities of pure MXene, pure ZnO, and ZnO/Ti<sub>3</sub>C<sub>2</sub>T<sub>x</sub> with different MXene weight ratios were also recorded and shown in Figure 6. Figure 6a,b illustrates the response of ZT1, ZT2, ZT3, and pure MXene sensors to NO<sub>2</sub> concentrations at 5 ppm and 10 ppm, respectively. The response signal of pure ZnO did not detect at room temperature, indicating semiconductor characteristics. The response signals of all the sensors were enhanced with the increase of NO<sub>2</sub> concentration, while the response of pure Ti<sub>3</sub>C<sub>2</sub>T<sub>x</sub> MXene was not well developed with noise signals, due to metallic behavior. The responses to 5 and 10 ppm NO<sub>2</sub> were calculated at 35% and 54%, respectively. The NO<sub>2</sub> response and recovery properties of ZT2 at room temperature were more substantial than those of ZT1 and ZT3, which were inadequate (Figure 6b).

In addition, the saturation time of the ZnO/Ti<sub>3</sub>C<sub>2</sub>T<sub>x</sub> heterostructure to NO<sub>2</sub> was recorded. For this evaluation, the ZT2 sensor was exposed to NO<sub>2</sub> at a time interval of 5 min. After 10 min, the sensing signal seemed to be saturated, as shown in Figure 6c. For further clarification, Figure 6d displays the sensing response to 10ppm of various gases (e.g., H<sub>2</sub>, NH<sub>3</sub>, CH<sub>4</sub>, NO<sub>2</sub>, CO<sub>2</sub>) based on the ZnO/Ti<sub>3</sub>C<sub>2</sub>T<sub>x</sub> sensor. It can be observed that the ZT2 nanocomposite had the significant response to NO<sub>2</sub> in comparison with other gases at low and high humidity.

In order to further explore the sensing activities of ZnO/Ti<sub>3</sub>C<sub>2</sub>T<sub>x</sub> heterostructure to NO<sub>2</sub> gas molecules, the ZT2 sensor was exposed to various NO<sub>2</sub> concentrations ranging from 5 to 30 ppm. As illustrated in Figure 6e, the result increased with the rising concentration of NO<sub>2</sub>, exhibiting that the proposed ZT2 to NO<sub>2</sub> molecule was logarithmic with the linear regression (R<sup>2</sup>) of 0.992 was acquired. Moreover, the repeatable cycle to 5–30 ppm NO<sub>2</sub> molecules of the ZT2 sensor, provided in Figure 6f, reveals that the sensor possesses a repeatable characteristic. The gas sensing performance of Ti<sub>3</sub>C<sub>2</sub>T<sub>x</sub>-based sensors is summarized in Table 1. Although our ZnO/Ti<sub>3</sub>C<sub>2</sub>T<sub>x</sub> sensor did not show a remarkable NO<sub>2</sub> response compared with other sensors, it is a promising candidate for NO<sub>2</sub> detection at room temperature.

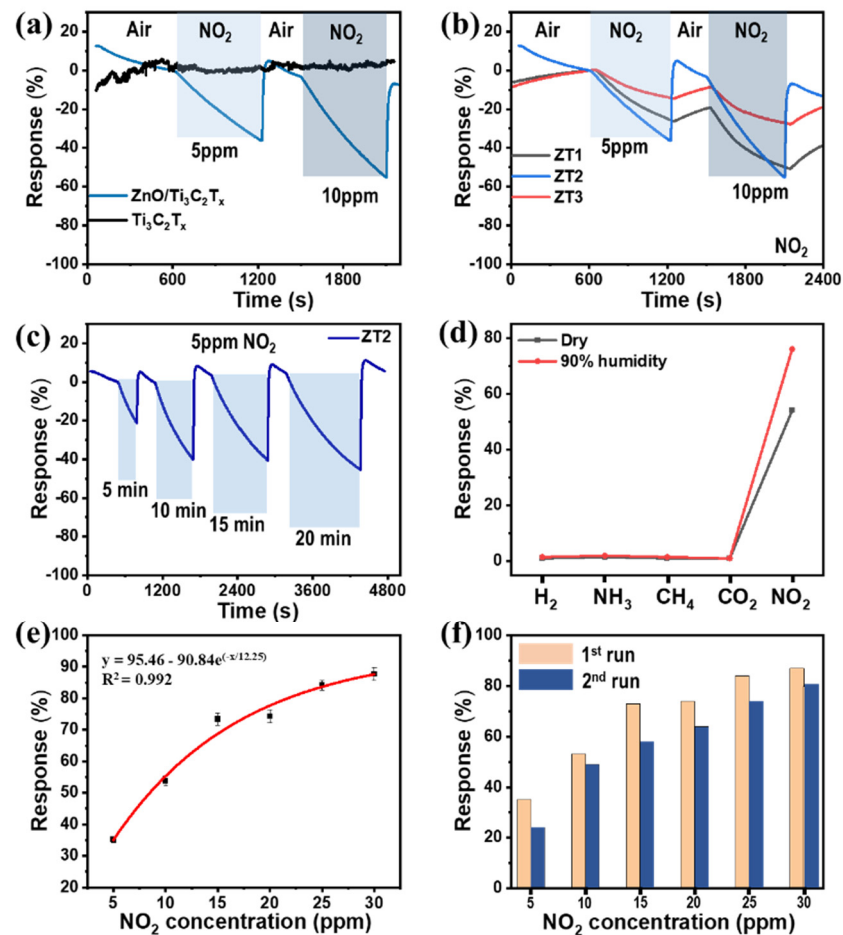


**Figure 6.** (a) NO<sub>2</sub> response curves of pure Ti<sub>3</sub>C<sub>2</sub>T<sub>x</sub> MXene and ZnO/Ti<sub>3</sub>C<sub>2</sub>T<sub>x</sub> nanocomposite (ZT2). (b) Comparison of NO<sub>2</sub> responses of ZT1, ZT2, and ZT3. (c) Cyclic responses of NO<sub>2</sub> gas at different times. (d) Comparison of responses of ZT2 sample to various gases at 10 ppm concentration. (e) Calibration curve of sensor response versus NO<sub>2</sub> concentration using logarithmic plot. (f) Cyclic responses of ZT2 to the different concentration of NO<sub>2</sub>.

**Table 1.** The comparison of NO<sub>2</sub> sensing in other materials, including Ti<sub>3</sub>C<sub>2</sub>T<sub>x</sub> MXene, was explored in previous literature.

Material	Temp. (°C)	Concentration (ppm)	Response (%)
2D MoS <sub>2</sub> /Ti <sub>3</sub> C <sub>2</sub> T <sub>x</sub> [16]	RT	10	25
3D crumpled Ti <sub>3</sub> C <sub>2</sub> T <sub>x</sub> /ZnO [20]	RT	20	22.5
2D/2D/2D Ti <sub>3</sub> C <sub>2</sub> T <sub>x</sub> @TiO <sub>2</sub> @MoS <sub>2</sub> [31]	RT	50	55
ZnO/Ti <sub>3</sub> C <sub>2</sub> T <sub>x</sub> nanocomposite *	RT	10	54

\* This work.

The improved NO<sub>2</sub> sensing activity of the nanocomposite was attributable to the creation of a heterogeneous p-n junction. When the ZnO/Ti<sub>3</sub>C<sub>2</sub>T<sub>x</sub> MXene nanocomposite sensor was exposed to the air, oxygen molecules were covered and captured by the electrons on the material layers, as shown in Figure 7. At room temperature, most adsorbed oxygen molecules tend to create negative oxygen species (O<sub>2</sub><sup>-</sup>, O<sup>2-</sup>, and O<sup>-</sup>) at defects and active sites of the sensor layers, which play a predominant part in improved gas sensing [33–35].

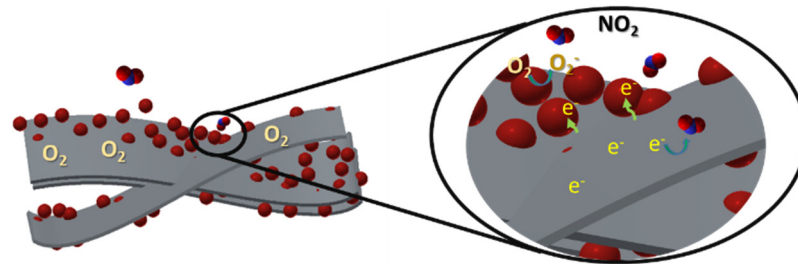
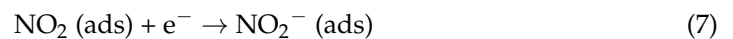


**Figure 7.** Schematic  $\text{NO}_2$ -sensing reaction mechanism of  $\text{ZnO}/\text{Ti}_3\text{C}_2\text{T}_x$  nanocomposite.

During the checking of  $\text{NO}_2$  sensing properties, it was expected that the  $\text{NO}_2$  gas would react with  $\text{O}_2^-$  species to form  $\text{NO}_3^-$  species, owing to the oxygen having lower electronegativity than the target gas [20,36,37]. Simultaneously,  $\text{NO}_2$  gas collected electrons and enhanced the depletion layer, thus improving the response and recovery values. Moreover,  $\text{NO}_2$  gas can be absorbed on the surface of p-type  $\text{Ti}_3\text{C}_2\text{T}_x$  MXene due to its oxidizing and electrophilic properties, resulting in reduced resistance [38]. Essentially,  $\text{ZnO}$  nanoparticles with an n-doping effect were decorated with a number of negative oxygen species ( $\text{O}_2^-$ ) on the surface and supported an important role in the absorption of  $\text{NO}_2$  [39]. Under ambient humidity, the hydrogen bonding between  $\text{NO}_2$  and  $\text{H}_2\text{O}$  molecules further promoted the chemical adsorption of  $\text{NO}_2$  [40]. The electron donation reaction can be described as follows [20,41,42]:



#### 4. Conclusions

In summary, the preparation of  $\text{ZnO}/\text{Ti}_3\text{C}_2\text{T}_x$  MXene nanocomposite by effective ultrasonication was investigated. In comparison with pure  $\text{ZnO}$  nanoparticles and  $\text{Ti}_3\text{C}_2\text{T}_x$  MXene, the optimized nanocomposite achieved sensitivity and selectivity to  $\text{NO}_2$  gas sensing. The response to 5 ppm  $\text{NO}_2$  was calculated at 35% with a speedy recovery and long-term stability at room temperature. The high sensitivity  $\text{NO}_2$  sensing activity of  $\text{ZnO}/\text{Ti}_3\text{C}_2\text{T}_x$  MXene nanocomposite was ascribed to the active sites and defects, which were the p-n heterointerface contacts between  $\text{ZnO}$  nanoparticles and  $\text{Ti}_3\text{C}_2\text{T}_x$  MXene. The results of this combination structure pave the way for the chemical sensing of  $\text{Ti}_3\text{C}_2\text{T}_x$  MXene-based materials, thus providing a reference by which to understand the fundamentals of  $\text{Ti}_3\text{C}_2\text{T}_x$  MXene gas sensing.

**Author Contributions:** Conceptualization, methodology, validation, formal analysis, investigation, resources, data curation, Q.T.H.T.; writing—original draft preparation, D.T.; writing—review and editing, visualization, supervision, project administration, funding acquisition, J.-S.N. All authors have read and agreed to the published version of the manuscript.

**Funding:** This research was funded by a National Research Foundation of Korea (NRF) grant funded by the Korean government (MSIT) (No. 2019R1A2C1008746).

**Institutional Review Board Statement:** Not applicable.

**Informed Consent Statement:** Not applicable.

**Data Availability Statement:** Not applicable.

**Conflicts of Interest:** The authors declare no conflict of interest.

## References

1. Nguyen, T.P.; Nguyen, D.M.T.; Le, H.K.; Vo, D.-V.N.; Lam, S.S.; Varma, R.S.; Shokouhimehr, M.; Nguyen, C.C.; Van Le, Q. MXenes: Applications in Electrocatalytic, Photocatalytic Hydrogen Evolution Reaction and CO<sub>2</sub> Reduction. *Mol. Catal.* **2020**, *486*, 110850. [[CrossRef](#)]
2. Anasori, B.; Gogotsi, Û.G. *2D Metal Carbides and Nitrides (MXenes)*; Springer: Berlin, Germany, 2019; ISBN 3030190269.
3. Thanh, Q.; Ta, H.; Tran, N.M.; Noh, J. Rice Crust-Like ZnO/Ti<sub>3</sub>C<sub>2</sub>T<sub>x</sub> MXene Hybrid Structures for Improved Photocatalytic Activity. *Catalysts* **2020**, *10*, 1140. [[CrossRef](#)]
4. Ta, Q.T.H.; Tran, N.M.; Noh, J.S. Pressureless Manufacturing of Cr<sub>2</sub>AlC Compound and the Temperature Effect. *Mater. Manuf. Process.* **2021**, *36*, 200–208. [[CrossRef](#)]
5. Anasori, B.; Lukatskaya, M.R.; Gogotsi, Y. 2D Metal Carbides and Nitrides (MXenes) for Energy Storage. *Nat. Rev. Mater.* **2017**, *2*, 16098. [[CrossRef](#)]
6. Thi, Q.V.; Patil, S.A.; Katkar, P.K.; Rabani, I.; Patil, A.S.; Ryu, J.; Kolekar, G.; Tung, N.T.; Sohn, D. Electrochemical Performance of Zinc-Based Metal-Organic Framework with Reduced Graphene Oxide Nanocomposite Electrodes for Supercapacitors. *Synth. Met.* **2022**, *290*, 117155. [[CrossRef](#)]
7. Li, X.; Bai, Y.; Shi, X.; Su, N.; Nie, G.; Zhang, R.; Nie, H.; Ye, L. Applications of MXene (Ti<sub>3</sub>C<sub>2</sub>T<sub>x</sub>) in Photocatalysis: A Review. *Mater. Adv.* **2021**, *2*, 1570–1594. [[CrossRef](#)]
8. Thi, Q.V.; Nguyen, N.Q.; Oh, I.; Hong, J.; Koo, C.M.; Tung, N.T.; Sohn, D. Thorny Trunk-like Structure of Reduced Graphene Oxide/HKUST-1 MOF for Enhanced EMI Shielding Capability. *Ceram. Int.* **2021**, *47*, 10027–10034. [[CrossRef](#)]
9. Yan, L.; Luo, X.; Yang, R.; Dai, F.; Zhu, D.; Bai, J.; Zhang, L.; Lei, H. Highly Thermoelectric ZnO@MXene (Ti<sub>3</sub>C<sub>2</sub>T<sub>x</sub>) Composite Films Grown by Atomic Layer Deposition. *ACS Appl. Mater. Interfaces* **2022**, *14*, 34562–34570. [[CrossRef](#)]
10. Lee, Y.; Kim, S.J.; Kim, Y.J.; Lim, Y.; Chae, Y.; Lee, B.J.; Kim, Y.T.; Han, H.; Gogotsi, Y.; Ahn, C.W. Oxidation-Resistant Titanium Carbide MXene Films. *J. Mater. Chem. A* **2020**, *8*, 573–581. [[CrossRef](#)]
11. Ta, Q.T.H.; Cho, E.; Sreedhar, A.; Noh, J.-S. Mixed-Dimensional, Three-Level Hierarchical Nanostructures of Silver and Zinc Oxide for Fast Photocatalytic Degradation of Multiple Dyes. *J. Catal.* **2019**, *371*, 1–9. [[CrossRef](#)]
12. Sreedhar, A.; Ta, Q.T.H.; Noh, J.-S. Advancements in the Photocatalytic Activity of Various Bismuth-Based Semiconductor/Ti<sub>3</sub>C<sub>2</sub> MXene Interfaces for Sustainable Environmental Management: A Review. *J. Ind. Eng. Chem.* **2022**, *115*, 26–47. [[CrossRef](#)]
13. Shahzad, F.; Alhabeab, M.; Hatter, C.B.; Anasori, B.; Man Hong, S.; Koo, C.M.; Gogotsi, Y. Electromagnetic Interference Shielding with 2D Transition Metal Carbides (MXenes). *Science* **2016**, *353*, 1137–1140. [[CrossRef](#)]
14. Van Ngoc, H.; Pham, K.D. First-Principles Study on N<sub>2</sub>, H<sub>2</sub>, O<sub>2</sub>, NO, NO<sub>2</sub>, CO, CO<sub>2</sub>, and SO<sub>2</sub> Gas Adsorption Properties of the Sc<sub>2</sub>CF<sub>2</sub> Monolayer. *Phys. E Low-Dimens. Syst. Nanostruct.* **2022**, *141*, 115162. [[CrossRef](#)]
15. Nguyen, T.D.; Lee, J.S. Electrospinning-Based Carbon Nanofibers for Energy and Sensor Applications. *Appl. Sci.* **2022**, *12*, 6048. [[CrossRef](#)]
16. Ta, Q.T.H.; Tri, N.N.; Noh, J.-S. Improved NO<sub>2</sub> Gas Sensing Performance of 2D MoS<sub>2</sub>/Ti<sub>3</sub>C<sub>2</sub>T<sub>x</sub> MXene Nanocomposite. *Appl. Surf. Sci.* **2022**, *604*, 154624.
17. Mohammadi, A.V.; Rosen, J.; Gogotsi, Y. The World of Two-Dimensional Carbides and Nitrides (MXenes). *Science* **2021**, *372*, eabf1581. [[CrossRef](#)]
18. Ta, Q.T.H.; Tran, N.M.; Tri, N.N.; Sreedhar, A.; Noh, J.-S. Highly Surface-Active Si-Doped TiO<sub>2</sub>/Ti<sub>3</sub>C<sub>2</sub>T<sub>x</sub> Heterostructure for Gas Sensing and Photodegradation of Toxic Matters. *Chem. Eng. J.* **2021**, *425*, 131437. [[CrossRef](#)]
19. Zhao, L.; Wang, K.; Wei, W.; Wang, L.; Han, W. High-performance Flexible Sensing Devices Based on Polyaniline/MXene Nanocomposites. *InfoMat* **2019**, *1*, 407–416. [[CrossRef](#)]
20. Yang, Z.; Jiang, L.; Wang, J.; Liu, F.; He, J.; Liu, A.; Lv, S.; You, R.; Yan, X.; Sun, P. Flexible Resistive NO<sub>2</sub> Gas Sensor of Three-Dimensional Crumpled MXene Ti<sub>3</sub>C<sub>2</sub>T<sub>x</sub>/ZnO Spheres for Room Temperature Application. *Sens. Actuators B Chem.* **2021**, *326*, 128828. [[CrossRef](#)]
21. Thi, Q.V.; Ko, J.; Jo, Y.; Joo, Y. Ion-Incorporative, Degradable Nanocellulose Crystal Substrate for Sustainable Carbon-Based Electronics. *ACS Appl. Mater. Interfaces* **2022**, *14*, 43538–43546. [[CrossRef](#)]
22. Wang, R.; Li, M.; Sun, K.; Zhang, Y.; Li, J.; Bao, W. Element-Doped Mxenes: Mechanism, Synthesis, and Applications. *Small* **2022**, *18*, 2201740. [[CrossRef](#)]
23. My Tran, N.; Thanh Hoai Ta, Q.; Sreedhar, A.; Noh, J.S. Ti<sub>3</sub>C<sub>2</sub>T<sub>x</sub> MXene Playing as a Strong Methylene Blue Adsorbent in Wastewater. *Appl. Surf. Sci.* **2021**, *537*, 148006. [[CrossRef](#)]
24. Sreedhar, A.; Ta, Q.T.H.; Noh, J.-S. Rational Engineering of Morphology Modulated Ti-ZnO Thin Films Coupled Monolayer Ti<sub>3</sub>C<sub>2</sub> MXene for Efficient Visible Light PEC Water Splitting Activity. *J. Electroanal. Chem.* **2022**, *921*, 116703. [[CrossRef](#)]
25. Bahng, J.H.; Yeom, B.; Wang, Y.; Tung, S.O.; Hoff, J.D.; Kotov, N. Anomalous Dispersions of “hedgehog” Particles. *Nature* **2015**, *517*, 596–599. [[CrossRef](#)]
26. Tran, N.M.; Ta, Q.T.H.; Noh, J.-S. RGO/Ti<sub>3</sub>C<sub>2</sub>T<sub>x</sub> Heterostructures for the Efficient, Room-Temperature Detection of Multiple Toxic Gases. *Mater. Chem. Phys.* **2021**, *273*, 125087. [[CrossRef](#)]

27. Ta, Q.T.H.; Namgung, G.; Noh, J.S. Synthesis of Ag@rGO/g-C<sub>3</sub>N<sub>4</sub> Layered Structures and Their Application to Toxic Gas Sensors: Effect of Ag Nanoparticles. *Electron. Mater. Lett.* **2019**, *15*, 750–759. [[CrossRef](#)]
28. Thanh Hoai Ta, Q.; Park, S.; Noh, J.-S. Ag Nanowire/ZnO Nanobush Hybrid Structures for Improved Photocatalytic Activity. *J. Colloid Interface Sci.* **2017**, *505*, 437–444. [[CrossRef](#)]
29. Kim, J.-H.; Ta, Q.T.H.; Noh, J.-S. Highly Strain-Tolerant, Disposable Gas Sensor on Plastic Wrap Using Two-Dimensional Hybrid Nanomaterials. *Mater. Chem. Phys.* **2022**, *292*, 126820. [[CrossRef](#)]
30. Nguyen, N.T.A.; Kim, H. Ag<sub>3</sub>PO<sub>4</sub>-Deposited TiO<sub>2</sub>@Ti<sub>3</sub>C<sub>2</sub> Petals for Highly Efficient Photodecomposition of Various Organic Dyes under Solar Light. *Nanomaterials* **2022**, *12*, 2464. [[CrossRef](#)]
31. Liu, Z.; Lv, H.; Xie, Y.; Wang, J.; Fan, J.; Sun, B.; Jiang, L.; Zhang, Y.; Wang, R.; Shi, K. A 2D/2D/2D Ti<sub>3</sub>C<sub>2</sub>T<sub>x</sub>@TiO<sub>2</sub>@MoS<sub>2</sub> Heterostructure as an Ultrafast and High-Sensitivity NO<sub>2</sub> Gas Sensor at Room-Temperature. *J. Mater. Chem. A* **2022**, *10*, 11980–11989. [[CrossRef](#)]
32. Bui, H.T.; Van Thuan, D.; Huong, P.T.; Nguyen, K.D.; Nguyen, M.V.; Chu, T.T.H.; Van Le, Q.; Jitae, K.; Devanesan, S.; AlSalhi, M.S. Enhanced Photocatalytic H<sub>2</sub> Evolution and Photodegradation of Antibiotic Tetracycline in Wastewater by TiO<sub>2</sub>@Ti<sub>3</sub>C<sub>2</sub>. *Int. J. Hydrogen Energy*, 2022, in press. [[CrossRef](#)]
33. Ji, H.; Zeng, W.; Li, Y. Gas Sensing Mechanisms of Metal Oxide Semiconductors: A Focus Review. *Nanoscale* **2019**, *11*, 22664–22684. [[CrossRef](#)]
34. Li, Z.; Yao, Z.; Haidry, A.A.; Plecenik, T.; Xie, L.; Sun, L.; Fatima, Q. Resistive-Type Hydrogen Gas Sensor Based on TiO<sub>2</sub>: A Review. *Int. J. Hydrogen Energy* **2018**, *43*, 21114–21132. [[CrossRef](#)]
35. Zhu, Y.; Ma, Y.; Wu, D.; Jiang, G. Preparation and Gas Sensing Properties of ZnO/MXene Composite Nanomaterials. *Sensors Actuators A Phys.* **2022**, *344*, 113740. [[CrossRef](#)]
36. Rzajj, J.M.; Abass, A.M. Review on: TiO<sub>2</sub> Thin Film as a Metal Oxide Gas Sensor. *J. Chem. Rev.* **2020**, *2*, 114–121. [[CrossRef](#)]
37. Wu, M.; He, M.; Hu, Q.; Wu, Q.; Sun, G.; Xie, L.; Zhang, Z.; Zhu, Z.; Zhou, A. Ti<sub>3</sub>C<sub>2</sub> MXene-Based Sensors with High Selectivity for NH<sub>3</sub> Detection at Room Temperature. *ACS Sens.* **2019**, *4*, 2763–2770. [[CrossRef](#)]
38. Kim, S.J.; Koh, H.-J.; Ren, C.E.; Kwon, O.; Maleski, K.; Cho, S.-Y.; Anasori, B.; Kim, C.-K.; Choi, Y.-K.; Kim, J. Metallic Ti<sub>3</sub>C<sub>2</sub>T<sub>x</sub> MXene Gas Sensors with Ultrahigh Signal-to-Noise Ratio. *ACS Nano* **2018**, *12*, 986–993. [[CrossRef](#)]
39. Doan, T.H.P.; Ta, Q.T.H.; Sreedhar, A.; Hang, N.T.; Yang, W.; Noh, J.-S. Highly Deformable Fabric Gas Sensors Integrating Multidimensional Functional Nanostructures. *ACS Sens.* **2020**, *5*, 2255–2262. [[CrossRef](#)]
40. Bhati, V.S.; Kumar, M.; Banerjee, R. Gas Sensing Performance of 2D Nanomaterials/Metal Oxide Nanocomposites: A Review. *J. Mater. Chem. C* **2021**, *9*, 8776–8808. [[CrossRef](#)]
41. Nazemi, H.; Joseph, A.; Park, J.; Emadi, A. Advanced Micro-and Nano-Gas Sensor Technology: A Review. *Sensors* **2019**, *19*, 1285. [[CrossRef](#)] [[PubMed](#)]
42. Thi, Q.V.; Park, S.; Jeong, J.; Lee, H.; Hong, J.; Koo, C.M.; Tung, N.T.; Sohn, D. A Nanostructure of Reduced Graphene Oxide and NiO/ZnO Hollow Spheres toward Attenuation of Electromagnetic Waves. *Mater. Chem. Phys.* **2021**, *266*, 124530. [[CrossRef](#)]